land

MDPI

*Article*

# Spatiotemporal Patterns of the Evolution of the Urban Heat Island Effect and Population Heat Exposure Risks in Xi'an, One of China's Megacities, from 2003 to 2023

**Zijie Li [1,†], Xinqi Wang [2,†], Haiyue Zhao [1] and Xiaoming Xu [1,*]**

[1] Department of Landscape Architecture, School of Landscape Architecture, Beijing Forestry University, Beijing 100083, China; lzj040413@bjfu.edu.cn (Z.L.); laphdzhy@bjfu.edu.cn (H.Z.)
[2] NUS College of Design and Engineering, National University of Singapore, Singapore 117565, Singapore; e1538074@u.nus.edu
* Correspondence: xuxiaoming@bjfu.edu.cn
† These authors contributed equally to this work.

**Abstract**

Under the dual pressure of rapid urbanization and global warming, the urban heat island (UHI) effect has been intensifying, accompanied by a continuous increase in heat exposure. As a typical example of rapid urbanization in China, Xi'an is facing severe challenges. However, previous research on diurnal variations in long-term UHI effects and heat risks is insufficient. So, this study utilized the temperature level threshold method and the heat exposure risk assessment model to investigate the spatiotemporal evolution characteristics of diurnal variations in the UHI and population heat exposure risks in Xi'an from 2003 to 2023. The results indicate that (1) over the past two decades, both the summer UHI intensity and the population heat exposure risks in Xi'an exhibited an overall intensifying trend, (2) spatial expansion followed a radial diffusion pattern centered on the urban core, with heat risk levels decreasing outward, (3) the nighttime expansion of high-level UHI zones and risk areas was slightly less than during the daytime, and (4) changes in the thermal environment often preceded population aggregation, indicating a lag effect in the evolution of heat exposure risks. This study deepened the understanding of the UHI and heat exposure for governments and planners and can help propose scientific UHI mitigation measures.

**Keywords:** heat exposure; metropolis; spatial expansion; thermal environment; urban heat islands

check for updates

Academic Editors: Gareth Rees and Liliia Hebryn Baidy

Received: 28 August 2025
Revised: 28 September 2025
Accepted: 29 September 2025
Published: 9 October 2025

**Citation:** Li, Z.; Wang, X.; Zhao, H.; Xu, X. Spatiotemporal Patterns of the Evolution of the Urban Heat Island Effect and Population Heat Exposure Risks in Xi'an, One of China's Megacities, from 2003 to 2023. *Land* **2025**, *14*, 2021. https://doi.org/10.3390/land14102021

**Copyright:** © 2025 by the authors. Licensee MDPI, Basel, Switzerland. This article is an open access article distributed under the terms and conditions of the Creative Commons Attribution (CC BY) license (https://creativecommons.org/licenses/by/4.0/).

## 1. Introduction

In the process of rapid urbanization, dense buildings and large areas of impervious artificial surfaces have increasingly replaced green spaces as the dominant components of the urban underlying surface. Combined with greenhouse gas emissions generated by human activities, this has led to a significant increase in the absorption and storage of solar radiation in urban areas [1], resulting in consistently higher temperatures in cities compared with surrounding rural areas—a phenomenon known as the urban heat island (UHI) [2]. With rapid global urbanization, the UHI has emerged as a critical urban climate challenge. Numerous studies have shown that many densely populated cities, such as Berlin, London, Chongqing, and Shanghai, exhibit a significant UHI phenomenon [3–6]. Today, the UHI effect and the risk of exposing urban populations to extreme heat have

become one of the most important environmental issues that significantly constrain the sustainable development of cities.

The negative impacts of the UHI are both extensive and far-reaching. From a climatic perspective, the UHI alters local climate patterns within cities [7]. It increases the frequency and intensity of extreme weather events through its interaction with precipitation patterns [8–10]. Moreover, the UHI interacts with air pollution by accelerating the chemical reactions of pollutants at high temperatures, thereby exacerbating air quality issues [11–13]. Research has also demonstrated that UHI-induced high temperatures significantly elevate the risk of heat strains [14] and that prolonged exposure to high temperatures in the summer months can lead to a significant increase in acute cardiovascular health risks [15,16], with particular threat to the elderly, children, and the chronically ill. Mortality from heat-related illnesses increases dramatically in cities during heat waves [17,18]. Additionally, in tropical and subtropical regions, heat exposure reduces labor productivity and increases economic costs due to higher air-conditioning energy demands, ultimately impairing urban productivity and economic efficiency [19].

Previous research on the UHI has yielded substantial insights using ground-based meteorological observations, numerical simulations, and satellite remote sensing. These studies explored the spatiotemporal characteristics, formation mechanisms, and driving factors of the UHI [20–25]. Early investigations mainly focused on the calculation and spatial distribution of the UHI intensity, linking it to city size [26], population density [27], and land use type [28], while highlighting the mitigating roles of green infrastructure and a decentralized population distribution [29]. More recent studies have examined the temporal dynamics of the UHI, including its diurnal [30], seasonal [31], and inter-annual variation [32]. Studies have shown that the intensity of the UHI is usually stronger at night than during the day and stronger in winter than in summer and that the heat island effect can have some positive impacts in winter in some high-latitude cities [33,34]. Meanwhile, there has been an increase in research on the formation mechanism of the UHI effect, and recent studies have identified changes in the nature of the subsurface [35], anthropogenic heat source emissions [36,37] and the accumulation of atmospheric pollutants [38] as the main factors leading to the UHI effect.

Despite these advances, several gaps remain. Temporally, while many studies have addressed diurnal and seasonal changes in the UHI, systematic analyses over long time-series periods (e.g., over 20 years) are still limited [39], which has made it difficult to comprehensively understand the evolution of the urban heat island effect in response to long-term urbanization. Given that urbanization is a dynamic and continuous process, long time-series studies are essential for assessing how UHI changes with urban expansion and population growth. Furthermore, the existing research has focused solely on the UHI itself—emphasizing urban–rural temperature differences—without adequately identifying the direct threats to urban populations [40]. Research has shown that there will be a threat to human health only when a large number of people live in a city where the temperature exceeds the physiological threshold of human tolerance [6]. Therefore, mitigating the impact of extreme heat requires an integrated analysis of the UHI and population heat exposure. However, research that combines the spatiotemporal dynamics of a population with UHI exposure remains limited. Effective heat mitigation strategies within urban governance frameworks require long-term dynamic monitoring of both the UHI and UHI exposure; yet such dynamic perspectives are still lacking [41].

As a typical example of rapid urbanization, the city of Xi'an is facing a series of challenges brought about by the increasingly severe urban heat island effect. Over the past 20 years, the built-up area of Xi'an has expanded to more than three times its original size [42,43]. By the end of 2023, the resident population of Xi'an had exceeded 13 million,

with an urbanization rate of 79.88% [44]. Xi'an had experienced 10 extreme heat events, with the longest lasting 14 days [45]. In June 2022, Xi'an experienced a thermal anomaly during which the temperature exceeded 40 °C for 72 h [46]. According to the Master Plan of Territorial Spatial Development of Xi'an (2021–2035), Xi'an is currently in the key stage of building an essential central city in western China. The superimposed effects of the expansion of the built-up area and climate warming have made it challenging to manage the heat island problem, which makes it urgent to carry out a targeted study in this context.

This study took 2003–2023 as the research period and processed and analyzed satellite remote sensing images over multiple time periods to do the following: (1) analyzed the spatial and temporal evolution of summer heat island intensity in Xi'an city based on satellite remote sensing images and revealed its regional differences and diurnal characteristics; (2) integrated demographic data and thermal environmental information to quantify the spatial changes in the risk of heat exposure of the population and elucidated the scale of its diurnal differences; and (3) assessed the impacts of population growth and UHI intensification on heat risk. This research aims to deepen the understanding of long-term changes in UHI and UHI exposure under rapid urbanization, offering new perspectives on urban thermal environments. It provides a scientific foundation for improving thermal conditions, optimizing urban planning, and protecting public health in Xi'an, while serving as a valuable reference for other cities addressing climate change and pursuing sustainable development.

## 2. Materials and Methods

### *2.1. Study Area*

As an essential central city in western China, Xi'an is located in the Guanzhong Plain in the middle of the Yellow River Basin in the hinterland of mainland China (107.4–109.5° E, 33.4–34.5° N), with a total area of 10,097.01 km$^2$ (Figure 1a). The topography of Xi'an spans two geographical units, the Qinling fold belt and the North China Plateau, with the overall terrain gradually sloping from south to north, and the city's elevation ranges from about 380 to 3000 m above sea level. The main urban area of Xi'an is situated on the Weihe Plain, a relatively low and flat region. In terms of climate, Xi'an has a warm temperate semi-humid continental monsoon climate with distinct seasons. Winters are cold with little precipitation, while summers are hot and rainy. The annual average temperature ranges from 13.1 °C to 15.0 °C. The average temperature in January ranges from −1.2 °C to 0.7 °C, while the average temperature in July is 26.9 °C to 27.5 °C. The highest recorded temperature was 43.4 °C on 19 June 1966.

According to the Master Plan of Territorial Spatial Development of Xi'an (2021–2035), Xi'an has a permanent population of 13.17 million, and the urban development areas are primarily concentrated in Beilin, Lianhu, Xincheng, Yanta, and Chang'an districts, which together constitute the central urban area of Xi'an (Figure 1b). The central urban area covers a total area of approximately 759.36 km$^2$, accounting for only 7.5% of the city's total area. However, the permanent resident population of the central urban area reaches approximately 7.85 million, accounting for 59% of the city's total permanent resident population. Beyond the central urban area, the western region of Xi'an primarily serves functions related to high-tech industries and scientific research innovation. In contrast, the eastern and northern areas are responsible for cultural tourism, ecological agriculture, and advanced manufacturing. The Qinling Mountains in the southern region serve as a significant ecological barrier for Xi'an.

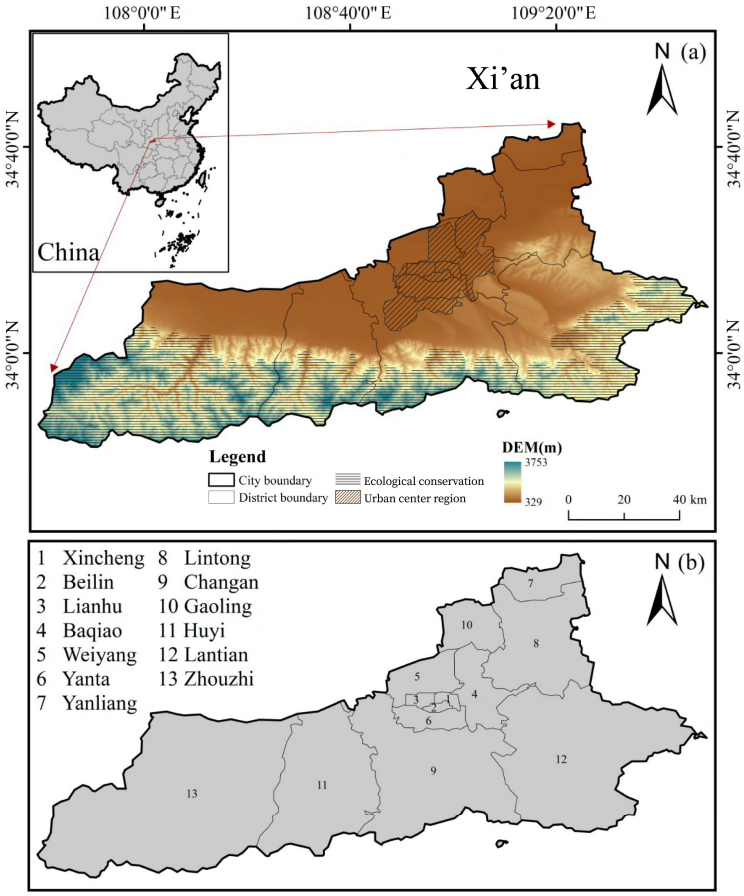


**Figure 1.** Location of the study area: (**a**) the topographic map; (**b**) the locations of all administrative districts.

### *2.2. Data Source and Preprocessing*

The main data used in this study include LST and population data.

In this study, we obtained daytime and nighttime LST data for summer (June–August) for five time periods (2003, 2008, 2013, 2018, and 2023) from the MOD11A2 product released by MODIS (provided by NASA's Terra and Aqua satellites, with land confidence levels of >95% and coverage of $\leq$2 km), which is a 8-day composite product with a spatial resolution of 1 km $\times$ 1 km (available on the GoogleEarthEngine cloud platform at https://code.earthengine.google.com/, accessed on 2 July 2025); the data were acquired through a dataset-specific API interface. MOD11A2 is generated by selecting the best-quality observations within each 8-day cycle, thus effectively reducing the effects of clouds and atmospheric disturbances. The LST data are based on the thermal infrared band inversion of the Terra satellite MODIS sensor (sourced by NASA, Washington, DC, USA), which has been widely used in the study of UHI due to its high temporal resolution, wide coverage, and reliable accuracy [47–49]. To consider the significance of the UHI effect, the agglomeration of population distribution, and the differences in population heat exposure risk between day and night in Xi'an, LST data from June to August, when Xi'an has the highest temperatures, were selected as the data in this study, so as to better investigate the UHI effect in Xi'an and its associated heat exposure risk to the residents.

Population data for the five time periods (2003, 2008, 2013, 2018, and 2023) used in this study were derived primarily from LandScan Global population distribution data and census data. LandScan data have a spatial resolution of approximately 1 km and were developed by the Oak Ridge National Laboratory, USA (available at: https://landscan.ornl.gov/, accessed on 28 June 2025). They are widely used in environmental effects or risk

exposure studies [50–52]. However, LandScan data are based on estimates and projections from multiple sources, and the population size often differs from the total population of the census [53]. To ensure the accuracy of the data, we referred to the method of Zhao et al. (2024) [54] and corrected the data based on the household population in the Xi'an Statistical Yearbook [55]; refer to Supplementary Materials for further details.

### *2.3. Identification of UHI Spatiotemporal Distribution and Classification of UHI Intensity Levels*

In this study, the temperature level threshold method was used to determine the UHI boundaries and classify UHI intensity levels. Currently, heat island classification methods mainly include the following categories: the calculation method based on LCZ (Local Climate Zone) classification, which identifies heat islands by the difference in the mean LST values between built-up areas and other land cover types [56]; the traditional urban–rural LST difference method, which calculates the LST difference between urban and rural areas to determine the intensity of urban heat islands (SUHIs) [57]; and the temperature level threshold method, which directly analyses the distribution of LST spatial intensities and produces heat island maps, with a focus on the risk of UHI exposure and local temperature anomalies [58]. To obtain more accurate UHI boundaries and meet the needs of long time-series analyses, this study chose the temperature level threshold method to determine the boundaries of UHI and classify UHI intensity levels, which has flexible grading capabilities, is convenient for portraying the spatial gradient changes in urban surface temperature, improves the expression of the spatial heterogeneity of the thermal environment, and is easy to operate [54].

The steps of the method are as follows: firstly, we defined the $LST_{UHI}$ as the temperature threshold for the UHI boundary, calculated as the average LST of the study area plus one standard deviation. The area with an LST higher than this threshold was defined as the spatial extent of UHI. Subsequently, the standard deviation (std) of the surface temperature within the UHI was calculated, referring to the related study [6,54,59]; the UHI intensity was classified into four levels based on the relationship between the threshold and the standard deviation (Table 1). The specific classification criteria are as follows: when $LST_i$ is smaller than $LST_{UHI}$ + 1std, it is defined as a weak heat island; when $LST_i$ is between $LST_{UHI}$ + 1std and $LST_{UHI}$ + 2std, it is defined as a moderate heat island; when $LST_i$ is between $LST_{UHI}$ + 2std and $LST_{UHI}$ + 3std, it is defined as a strong heat island; and when $LST_i$ is greater than or equal to $LST_{UHI}$ + 3std, it is defined as an extreme heat island [54].

**Table 1.** The classification of UHI intensity based on the mean–std method.

| UHI Intensity Levels | LST Ranges |
|---|---|
| Weak UHI | $LST_i < LST_{UHI} + 1std$ |
| Moderate UHI | $LST_{UHI} + 1std \leq LST_i < LST_{UHI} + 2std$ |
| Strong UHI | $LST_{UHI} + 2std \leq LST_i < LST_{UHI} + 3std$ |
| Extreme UHI | $LST_i \geq LST_{UHI} + 3std$ |

$LST_{UHM}$ is the temperature threshold for UHI boundary recognition, std is the standard deviation of LST in UHI areas, and $LST_i$ is the land surface temperature of the raster i.

### *2.4. Framework for Identification and Assessment of Population Heat Exposure Risk Areas*

Population heat exposure is the result of the joint action of a high-temperature environment and population aggregation, which reflects the degree to which urban populations are affected by high temperatures. The risk of heat exposure can usually be assessed by modeling the relationship between temperature and population variables. In this study, a heat exposure risk assessment model [54] was introduced, and the methodology of this model assessment consisted of two main sub-steps: (1) calculating the thermal comfort

index and (2) combining the thermal comfort index with demographic data to assess the population heat exposure.

In this study, the discomfort index (DI) was used to measure the level of physical comfort of the population in different thermal environments. The conventional calculation of the DI relies on air temperature data. Still, given that there is a high degree of consistency between the land surface temperature (LST) and the air temperature, and that regression analyses have verified a good correlation between the two, the LST can be used as a substitute for air temperature for the calculation of the DI in a large-scale regional analysis [60].

In this study, the urban discomfort index (UDI) was defined as the discomfort level of body sensation within the heat island. Referring to the conclusion of Wu et al. and previous studies [61,62], people can feel thermal comfort in non-UHI areas below the heat island temperature threshold, so the UDI value in non-UHI areas was set to 0. In UHI areas, people's thermal comfort gradually decreased with the increase in the UHI intensity, so the LST data in UHI areas were standardized to obtain the UDI value, as shown in Equation (1) [54]. The calculation formula is expressed as follows:

$$\mathrm{UDI} = \begin{cases} 0, & \mathrm{LST} < \mathrm{LST_{UHI}} \\ \frac{\mathrm{LST}-\mathrm{LST_{MIN}}}{\mathrm{LST_{MAX}}-\mathrm{LST_{MIN}}}, & \mathrm{LST} \geq \mathrm{LST_{UHI}} \end{cases} \quad (1)$$

where LST denotes the surface temperature of an image element; $\mathrm{LST_{UHI}}$ is the temperature threshold used to identify the boundary of UHI; $\mathrm{LST_{MIN}}$ and $\mathrm{LST_{MAX}}$ are the minimum value and the maximum value of the surface temperature in UHI areas, respectively, and the range of the UDI is calculated to be 0 to 1.

Subsequently, the population data were combined with the UDI values to construct a population thermal exposure risk assessment model [63] with reference to a population-weighted model. The model is used to measure the relative importance of a raster in the overall heat exposure structure and reflects whether the area is a key area for heat exposure by comparing the heat exposure value of the raster with the weighted average of the whole area, which in turn reflects the relative risk level of heat exposure of the population in the area. Accordingly, the relative risk level of heat exposure of the population is calculated using Equation (2) [54]:

$$\mathrm{EUHI_{raster}} = \frac{\mathrm{P_i} \times \mathrm{UDI_i}}{\frac{1}{\mathrm{N}} \times \sum_{i=1}^{N} \mathrm{P_i} \times \mathrm{UDI_i}} \quad (2)$$

where $\mathrm{EUHI_{raster}}$ is the standardized population heat exposure index of the i-th raster; $\mathrm{P_i}$ is the population size of the i-th raster; $\mathrm{UDI_i}$ is the value of the urban discomfort index for the i-th raster within UHI areas; and N is the total number of rasters in the study area.

Based on the calculation results of the relative risk assessment method for heat exposure of the population, combined with the definition of extreme high temperature in the traditional heat exposure model, and with reference to the classification standards of other types of heat exposure risk of the population [6,54], the heat exposure area of the population was classified into five risk levels [64]. The specific classification standards are shown in (Table 2).

**Table 2.** The relative risk levels of UHI exposure.

| Relative Risk Levels | $\mathrm{EUHI_{raster}}$ Ranges |
|---|---|
| No risk | $\mathrm{EUHI_{raster}} \leq 0.5$ |
| Low risk | $0.5 < \mathrm{EUHI_{raster}} \leq 1.5$ |
| Medium risk | $1.5 < \mathrm{EUHI_{raster}} \leq 2.5$ |
| High risk | $2.5 < \mathrm{EUHI_{raster}} \leq 3.5$ |
| Very high risk | $3.5 < \mathrm{EUHI_{raster}}$ |

## 3. Results

### *3.1. Spatial and Temporal Characteristics of UHI*

#### 3.1.1. Temporal and Spatial Distribution of Daytime UHI

The study used the temperature level threshold method to obtain the spatial and temporal distribution and intensity grading of UHI in Xi'an from 2003 to 2023. In general, the distribution pattern of daytime heat islands in Xi'an was characterized by a gradual agglomeration and interconnection of large-scale core heat islands and scattered small heat islands (Figure 2a).

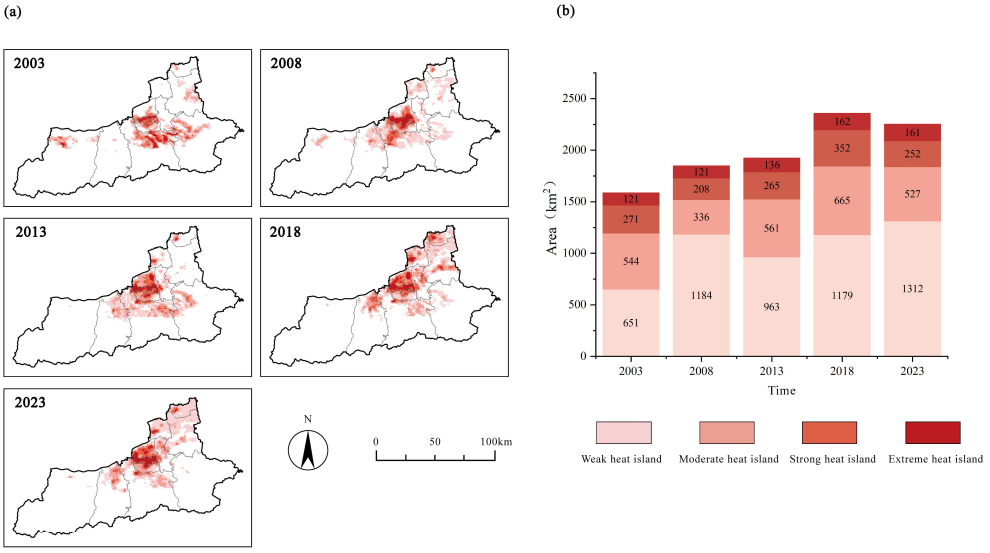


**Figure 2.** The spatial distribution and changes in daytime UHI extent in Xi'an from 2003 to 2023: (**a**) the spatial distribution of daytime UHI intensity levels in Xi'an at five-year intervals from 2003 to 2023; (**b**) the changes in daytime UHI areas of different intensities from 2003 to 2023.

During the study period, the total area of daytime heat islands in Xi'an grew from 1587 $km^2$ in 2003 to 1849 $km^2$ in 2008, then to 1925 $km^2$ in 2013, 2358 $km^2$ in 2018, and finally decreased to 2252 $km^2$ in 2023, with an overall growth rate of about 41.9%. Further calculations of the amount of change in the total daytime urban heat island area per 5 years were 262 $km^2$ (2003–2008), 76 $km^2$ (2008–2013), 433 $km^2$ (2013–2018) and −106 $km^2$ (2018–2023), which indicated that the urban heat island scale in Xi'an had experienced a staged trend of growth, followed by rapid expansion and then a slight decline (Figure 2b). From 2003 to 2013, the heat island primarily expanded along the urban development axis towards the east, southeast, and plains, with the area of medium and higher intensity heat islands increasing and the peripheral weak heat island patches increasing. After 2013, with the extension of urban construction to the Guanzhong Plain in the north and the Loess Plateau in the south, the expansion of heat islands to the north and southwest has been obvious, and since 2020, with the implementation of projects such as the construction of green areas, river wetland restoration, ecological protection of mountains, and urban regeneration in Xi'an, the expansion of the strong heat islands in the core area has slowed down. However, the range of weak and moderate heat islands has continued to expand. The core areas of major UHI were concentrated in the central and northern districts and counties and continued to expand outwards. At the same time, small UHI patches that used to be isolated were gradually connected to the main heat island clusters, and the spatial continuity of the high-temperature zone increased.

The results of the intensity grading of daytime Xi'an heat island areas showed obvious spatial differentiation characteristics. The area of weak heat islands increased from 651 $km^2$

in 2003 to 1312 km$^2$ in 2023. The area of medium heat islands grew from 544 km$^2$ in 2003 to a peak of 665 km$^2$ in 2018, then fluctuated and decreased to 527 km$^2$ in 2023, with the weak and moderate heat islands consistently distributed at the edges of the central urban area. Since the implementation of the "Western Development" strategy in the early 2000s, the northern part of Xi'an, especially the Weibei Region, has been positioned as an essential growth pole of the city, hosting a large number of industrial, manufacturing, and logistics facilities, including the Xi'an Economic and Technological Development Zone, the aviation industry base, and the Xi'an International Port Area. Therefore, a large number of weak and moderate intensity heat island areas appeared in north Xi'an during the daytime, which was closely related to the spatial development strategy, industrial agglomeration, and land use changes in the area in the past two decades.

The strong heat island area fluctuated and decreased from 271 km$^2$ in 2003 to 252 km$^2$ in 2023, which may have been related to the implementation of ecological restoration projects and urban greening initiatives. The area of very strong heat islands has been mainly concentrated in the centers of high-density built-up areas, i.e., Lianhu District, Beilin District, and Xincheng District, since 2003, and has remained relatively stable during the 20-year period, with a fluctuating area range of 121–162 km$^2$. From 2013 onwards, the distribution area of extreme heat islands, except for the central urban area, began to shift northeastward to Yanliang District and Gaoling District, Lintong District's regional centers, such as the district government seat and its surroundings, large residential areas, and other vital infrastructures, with a few strong and extreme urban heat island distributions.

#### 3.1.2. Temporal and Spatial Distribution of Nighttime UHI

During the study period, the total area of nighttime heat islands in Xi'an increased from 713 km$^2$ in 2003 to 838 km$^2$ in 2008, further increased to 981 km$^2$ in 2013, reached 1005 km$^2$ in 2018, and slightly decreased to 977 km$^2$ in 2023, with an overall increase of about 37%. The changes in the UHI area over each five-year interval were 125 km$^2$ (2003–2008), 143 km$^2$ (2008–2013), 24 km$^2$ (2013–2018), and −28 km$^2$ (2018–2023). These results indicated that the scale of nighttime UHI in Xi'an expanded continuously during the first decade, followed by a significant slowdown in growth and a minor contraction thereafter (Figure 3b). In terms of spatial expansion, the primary nighttime UHI core areas were concentrated in Lianhu District, Beilin District, and Weiyang District, with a general trend of outward diffusion toward peripheral zones and increasing spatial continuity. Between 2003 and 2008, nighttime UHI primarily expanded northwestward from the central urban area, as peripheral weak UHI zones gradually merged with the core clusters. Since 2013, the direction of expansion shifted, with UHI spreading radially outward along the city's urban development corridors (Figure 3a).

We further analyzed the spatial expansion trends of nighttime UHI of varying intensities in Xi'an. The area of weak nighttime UHI increased from 434 km$^2$ in 2003 to a peak of 552 km$^2$ in 2013, followed by a gradual decline to 459 km$^2$ in 2023. These weak UHIs were primarily distributed in the peripheral zones of the central urban area and at the edges of UHI expansion, appearing in fragmented patches, particularly in the western districts of Zhouzhi and E'yi. In contrast, the area of moderate UHI exhibited a continuous upward trend, expanding from 131 km$^2$ in 2003 to 284 km$^2$ in 2023. These zones primarily extended northward and northeastward along the city's development axes.

The spatial expansion patterns of strong and extreme UHI were similar to those of weak and moderate UHI. The area of strong UHI increased from 107 km$^2$ in 2003 to 175 km$^2$ in 2023, primarily concentrated near the central urban area and the core functional zones of newly developed districts. Extreme UHI remained concentrated in high-density built-up cores such as Lianhu, Beilin, and Xincheng districts, fluctuating between 41 and 80 km$^2$

over the years. Since 2018, a noticeable contraction trend has been observed in the spatial extent of extreme nighttime UHI, with such zones in the eastern part of Xincheng and Beilin districts nearly disappearing by 2023. While strong UHI in the core urban areas remained relatively stable, the moderate UHI zones in the periphery continued to expand outward.

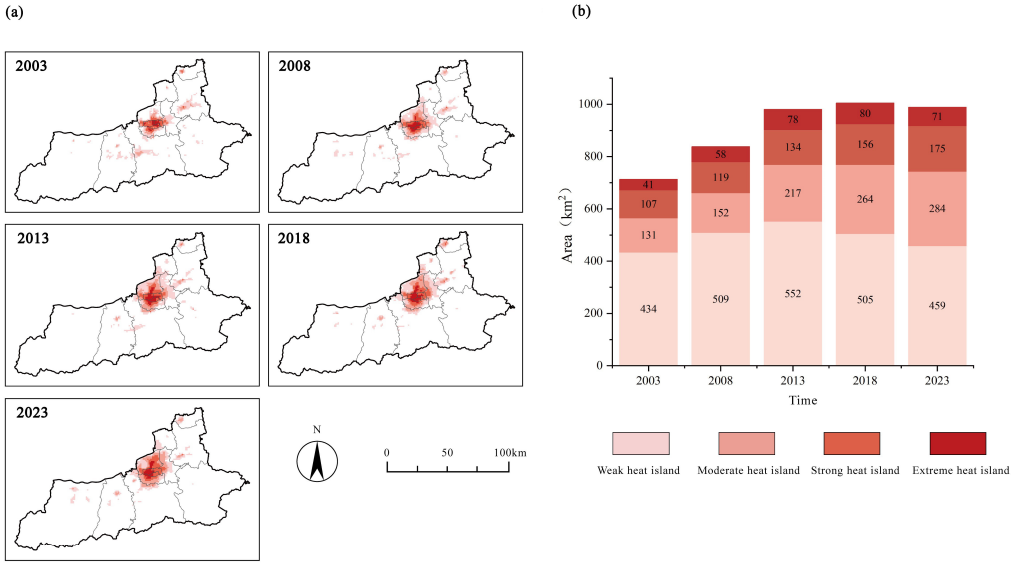


**Figure 3.** The spatial distribution and changes in nighttime UHI extent in Xi'an from 2003 to 2023: (**a**) the spatial distribution of nighttime UHI intensity levels in Xi'an at five-year intervals from 2003 to 2023; (**b**) the changes in nighttime UHI areas of different intensities from 2003 to 2023.

### *3.2. Spatial and Temporal Characteristics of Population Heat Exposure Risk*

#### 3.2.1. Temporal and Spatial Distribution of Population Heat Exposure Risk in Daytime

From 2003 to 2023, the proportion of population heat exposure risk zones in Xi'an exhibited pronounced diurnal dynamic variations. The distribution and temporal evolution of each risk level reflected the cumulative and escalating nature of urban heat exposure risk in the city over the past two decades.

From Figure 4b, it can be seen that the percentage of risk-free areas in Xi'an during daytime showed a fluctuating downward trend during 2003–2023, from 90.62% in 2003 to 92.16% in 2008, then gradually declined to 86.37% in 2018, and then slightly rebounded to 87.41% in 2023, with an overall reduction of 3.21 percentage points, and based on Figure 4a, it can be seen that the changes were mainly concentrated in the populated areas, which were the most critical areas in Xi'an. It can be seen that the changes were mainly concentrated in and around the central urban areas where the population was focused (Xincheng District, Beilin District, Lianhu District, Baqiao District, Weiyang District, and Yanta District), indicating that a large number of risk-free areas in the center of Xi'an were being transformed into risky areas. The proportion of low-risk areas, on the other hand, showed phased fluctuations, with 4.73% in 2003, which dropped to 3.20% in 2008, maintained a high level of around 6% from 2013 to 2018, and dropped back to 4.68% in 2023, reflecting frequent transformations of low-risk areas into risky areas of other grades. The share of medium-risk zones was on an overall upward trend, increasing from 1.45% in 2003 to 2.58% in 2018, and dropping slightly to 1.97% in 2023, which was still an increase of 0.52 percentage points from the initial period. The share of high-risk areas continued to expand, increasing from 0.52% in 2003 to 1.12% in 2018 and decreasing slightly to 1.11% in 2023, nearly triple from the initial period. The proportion of very-high-risk areas increased most significantly, from 2.68% in 2003 to 4.84% in 2023, representing an 80.81% increase.

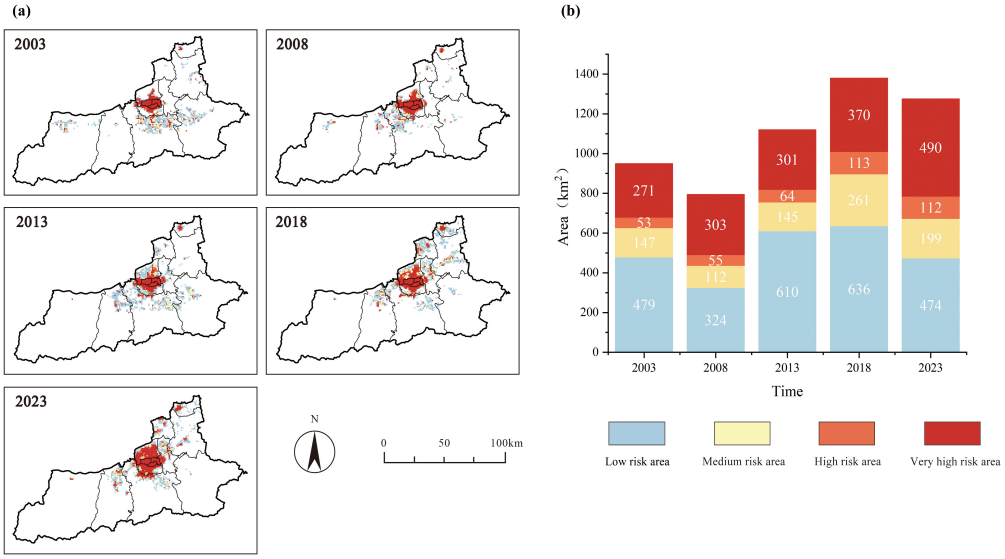


**Figure 4.** Risk distribution of daytime population heat exposure in Xi'an: (**a**) population heat exposure risk of daytime from 2003 to 2023; (**b**) the change in thermal risk area of daytime from 2003 to 2023.

### 3.2.2. Temporal and Spatial Distribution of Population Heat Exposure Risk at Night

From the distribution of heat exposure risk areas of 20 years in Figure 5a, the change trend of risk at nighttime in Xi'an showed some similarity to that during the daytime. From Figure 5b, it can be seen that the proportion of no-risk areas decreased continuously from 95.31% in 2003 to 92.39% in 2023, representing a decrease of 2.92 percentage points. The influence of heat exposure risk at night in the city center was expanding. The share of low-risk areas fluctuates less, remaining between 1.41 and 2.38 percent, falling to 1.82% in 2023, an increase of only 0.29 percentage points from 2003. The share of medium-risk regions increased from 0.53% in 2003 to 1.24% in 2018, falling slightly to 1.09% in 2023, an overall increase of 1.06 times. The share of high-risk regions has steadily increased, doubling from 0.31% in 2003 to 0.62% in 2023. The growth in the proportion of very-high-risk areas was particularly striking, increasing from 2.32% in 2003 to 4.09% in 2023, an increase of 76.17%, which was a central indicator of increased risk at night.

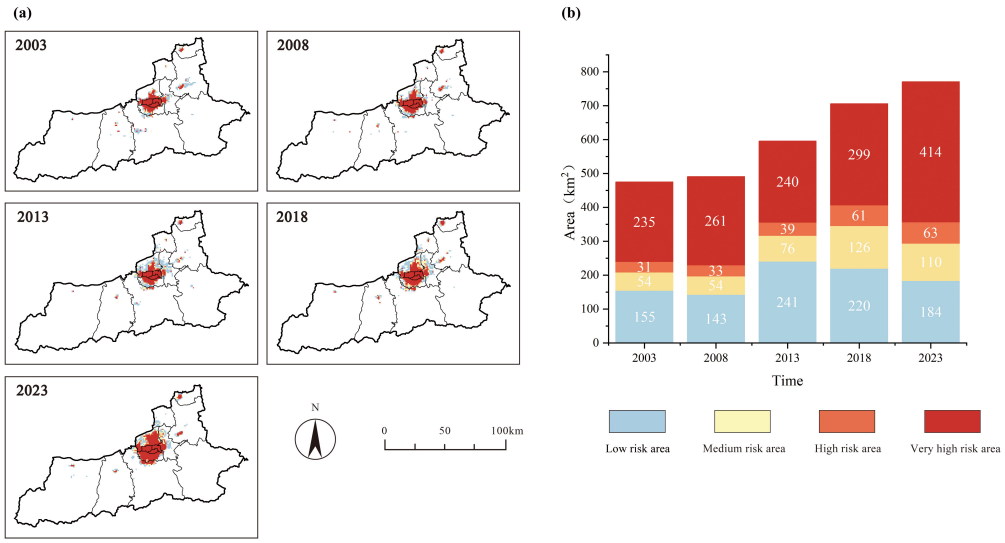


**Figure 5.** Risk distribution of nighttime population heat exposure in Xi'an: (**a**) population heat exposure risk at night from 2003 to 2023; (**b**) the change in thermal risk area at night from 2003 to 2023.

Comprehensive diurnal and nocturnal characteristics showed that the risk of heat exposure of the Xi'an population showed a significant trend of intensification from 2003 to 2023, which mainly manifested in the continuous expansion of the proportionate area of high-level risk zones (high risk and very high risk). Among them, the very-high-risk area increased by 0.81 times during the daytime and 0.76 times during the nighttime, respectively, and the growth rate was significantly accelerated in 2018–2023, indicating that the deterioration process of the thermal environment in Xi'an had accelerated in recent years. The transformation of risk zones at each level exhibited obvious escalation characteristics, and the transition from low-level to high-level risk zones occurred throughout the entire study period. The year 2018 was a significant peak risk node. In that year, the percentage of very-high-risk zones reached 3.65% during the daytime, the percentage of high-risk zones reached 1.12%, and the percentage of medium-risk zones reached 2.58%. The percentage of risky zones was at its peak in the observation period. Although the proportion of medium- and high-risk zones slightly decreased in 2023, the proportion of very-high-risk zones further jumped to 4.84%, a record high, indicating that the risk of heat exposure of Xi'an population had entered a substantial stage of intensification, and the rate of expansion of nighttime risk was gradually approaching the daytime level, so the management of the city's thermal environment was facing a serious challenge.

### *3.3. Space–Time Trend Pattern Division of UHI*

#### 3.3.1. Space–Time Trend Pattern Division of UHI in Daytime

From the spatial distribution trend of UHI in the daytime in Xi'an, the proportion of zones with no noticeable change in the intensity of the heat island area in Xi'an has been relatively high (Figure 6a).

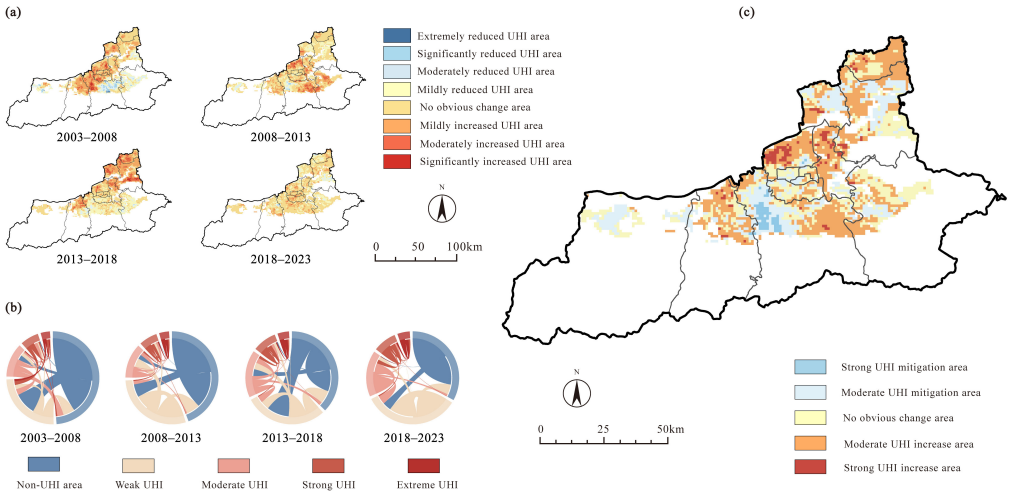


**Figure 6.** Spatiotemporal transfer and change trends of daytime UHI intensity areas. (**a**) UHI intensity distribution changed during the daytime over 5 years; (**b**) the mutual transformation between UHI regions with weak, moderate, strong, and extreme intensity levels and non-UHI regions during the daytime from 2003 to 2023; (**c**) the change in UHI area during the daytime from 2003 to 2023.

From 2003 to 2008, the areas transitioning into weak and moderate UHI zones were substantially larger than those transitioning out, primarily originating from non-UHI zones and low-intensity UHI regions (Figure 6b). In contrast, transitions between strong and extreme UHI categories were not significant. The main UHI intensification areas were concentrated within the six central districts. Meanwhile, a noticeable reduction in UHI intensity was observed in the southeastern part of the central city (northeastern Chang'an District and northern Lantian County), likely due to local greening and changes in land use. Between 2008 and 2013, all UHI categories experienced a greater area of inflow

than outflow, with more conversions from lower to higher intensity levels than in the opposite direction. UHI intensification expanded further into the northern and eastern regions, particularly around the Weibei industrial and development zones, where UHI intensity increased significantly. In the central city, the intensification range expanded, although a weakened UHI zone persisted in the southern area. From 2013 to 2018, UHI intensity significantly increased in the northern districts of Lintong, Yanliang, and Gaoling, forming a contiguous high-intensity zone. Intensification also expanded westward in the central city, while weakening in the south became less pronounced. Between 2018 and 2023, although the area of inflow for all UHI levels remained slightly greater than that of outflow, the inflow area showed a marked decline. UHI expansion and intensification were somewhat curbed, with the overall area of UHI intensification contracting compared with the previous period. Notably, weakening zones emerged at the northern and northwestern edges, which may be attributed to ecological restoration, green space development, and industrial restructuring. However, high UHI intensity persisted in the central city and parts of its northern surroundings.

Over the entire two-decade period (Figure 6c), areas with no significant change in daytime UHI intensity accounted for 10.2% of the total, while UHI mitigation zones represented 8.2%, UHI intensification zones 14.4%, significantly intensified UHI zones 0.7%, and significantly mitigated UHI zones 1.2%. Overall, Xi'an has exhibited a strengthening trend in daytime UHI intensity. However, the core urban areas did not show a clear trend of intensification. The significantly intensified UHI zones were mainly distributed in the Weiyang and Baqiao districts, forming a patchy distribution on the northern periphery of the central city. Notably, a continuously distributed UHI mitigation zone was identified in the southern part of the central city. This area has experienced a significant decrease in UHI intensity between 2003 and 2023, with spatial distribution dominated by strong and moderate mitigation levels. This was likely related to the ongoing development of numerous urban parks, green corridors, and ecological buffer zones in this region in recent years.

#### 3.3.2. Space–Time Trend Pattern Division of UHI at Night

Between 2003 and 2023, the nighttime UHI intensity in Xi'an exhibited relatively stable and spatially concentrated variation patterns (Figure 7a). From 2003 to 2008, the areas transitioned into weak and moderate UHI zones that significantly exceeded those that transitioned out, primarily originating from non-UHI and low-intensity UHI zones (Figure 7b). This indicated that during this period, nighttime UHIs expanded toward peripheral regions, with a gradual increase in low-intensity UHI areas. The primary zones of UHI intensification were located in the high-density built-up areas of the urban center, such as Lianhu District, Beilin District, and Xincheng District, as well as Weiyang District. In contrast, peripheral areas experienced insignificant changes in UHI intensity, with slight mitigation observed in parts of the southern and eastern fringe zones. Between 2008 and 2013, the scope of intensification expanded, particularly in Lintong District and Chang'an District, where UHI intensity increased notably, reflecting the northward expansion of urban development and industrial restructuring during this period. However, changes in the southwestern loess plateau remained minimal. From 2013 to 2023, the intensified UHI zones in the central urban area remained largely stable, with high levels of UHI intensity persisting in the core districts. This suggested that the thermal inertia of the nighttime urban thermal environment remained significant. Nevertheless, the intensification trend in the northeastern part of the city has markedly slowed.

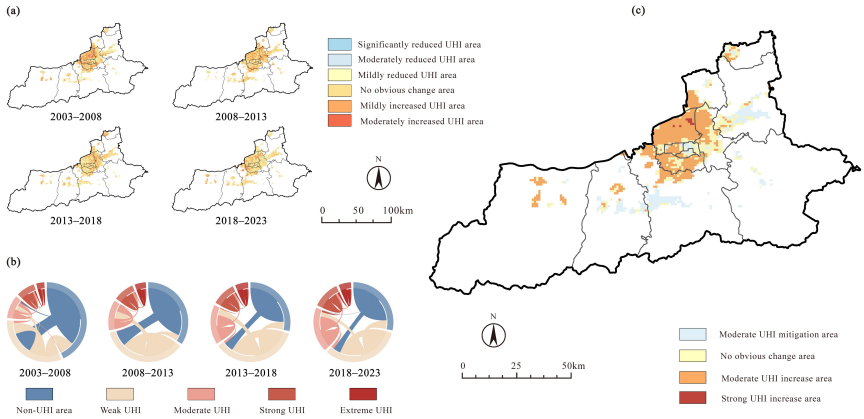


**Figure 7.** Spatiotemporal transfer and change trends of nighttime UHI intensity areas. (**a**) UHI intensity distribution changed at night over 5 years; (**b**) the mutual transformation between UHI regions with weak, moderate, strong, and extreme intensity levels and non-UHI regions at night from 2003 to 2023; (**c**) the change in UHI area at night from 2003 to 2023.

Over the past two decades, the spatial extent of nighttime UHI intensification has been relatively smaller compared with daytime UHI distribution (Figure 7c). Areas with no significant change in nighttime UHI intensity accounted for 4% of the city, while UHI mitigation zones made up 2.7%, UHI increase zones accounted for 7.1%, and significantly intensified UHI zones comprised only 0.08%. No areas experienced significant mitigation. Overall, nighttime UHI intensity exhibited a slight intensification trend; however, notable mitigation occurred in the major central urban areas. UHI phenomena in peripheral and sub-urban regions, particularly in the southern and western hilly zones, also weakened.

### *3.4. Space–Time Trend Pattern Division of Population*

From Figure 8a, it can be seen that most areas in Xi'an were sparsely populated, with population-dense areas and growth mainly concentrated in Beilin District, Lianhu District, Xincheng District, and Yanta District, exhibiting a trend of outward diffusion from these central zones. According to Figure 8b, during the 20 years following 2003, regions with no significant population change accounted for 83.7% of the total area. Areas with population decline accounted for 4.09%, while areas with population increase made up 11.38%. Additionally, areas with a significant population decrease and a significant increase accounted for 0.27% and 0.57%, respectively. Notably, population growth was primarily concentrated in the surrounding areas of the central urban districts.

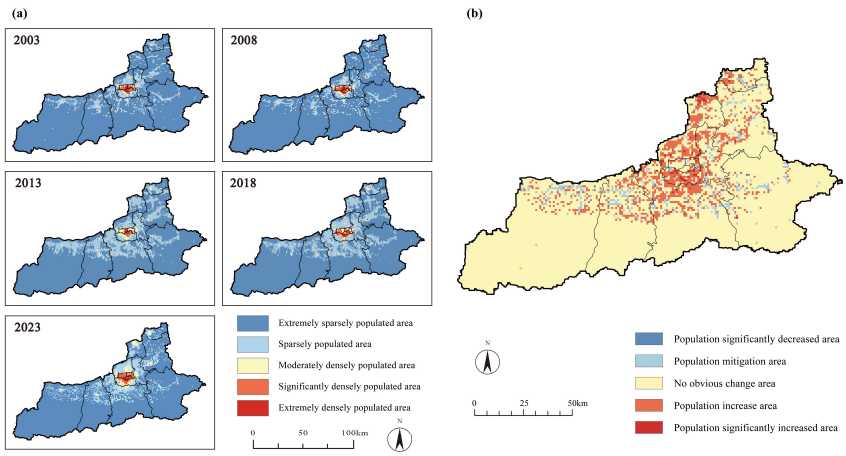


**Figure 8.** The space–time transfer and trend of population: (**a**) the population density of Xi'an from 2003 to 2023; (**b**) the change in population density from 2003 to 2023.

### *3.5. Space–Time Trend Pattern Division of Heat Exposure Risk*

#### 3.5.1. Space–Time Trend Pattern Division of Heat Exposure Risk in Daytime

Based on the area proportions of different risk levels shown in Figure 9a and 9b, the population heat exposure risk level in Xi'an has remained relatively stable in most areas, with a high proportion of regions experiencing no significant change. Between 2003 and 2008, the southeastern part of Xi'an showed a notable decrease in risk levels, while areas with increased risk were mainly concentrated within the central urban area. From 2008 to 2013, the southeastern part of the city experienced a significant increase in risk levels, indicating a shift in the population heat exposure risk hotspot from the city center to the southeastern periphery during daytime. Between 2013 and 2018, the risk hotspot shifted back to the city center and tended to expand northward. During the period from 2018 to 2023, areas with significantly elevated heat risk were again concentrated within the central urban area.

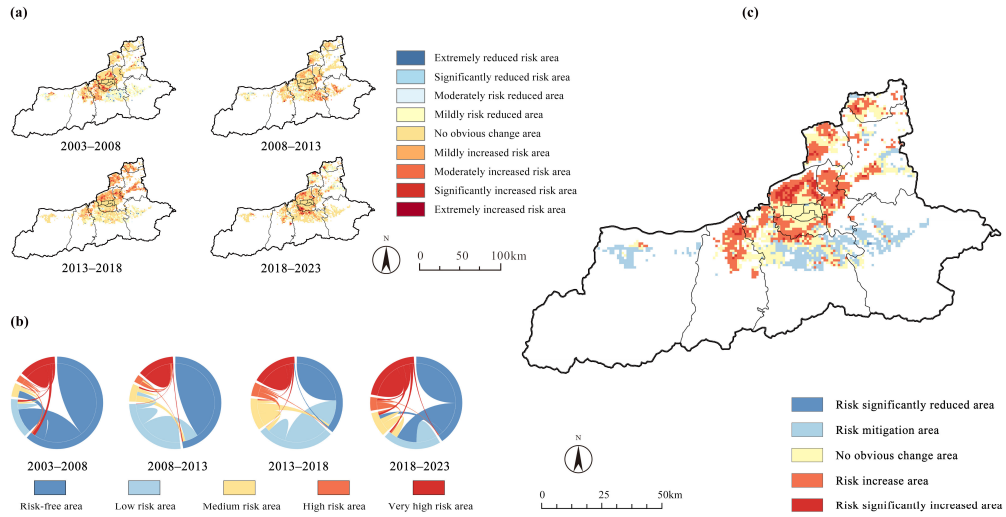


**Figure 9.** Spatial–temporal transfer and trend of heat exposure risk intensity of daytime population: (**a**) population heat exposure risk level changed of daytime in 5 years; (**b**) the mutual transformation between risk areas with low, medium, high, and very high risk levels and risk-free areas of daytime from 2003 to 2023; (**c**) the change in population heat exposure risk of daytime from 2003 to 2023.

As shown in Figure 9c, during the 20 years after 2003, the spatial distribution of daytime heat exposure risk in Xi'an was as follows: 7.95% of the area experienced no significant change, 5.24% saw a decrease in risk, 7.57% experienced an increase, 0.02% had a significant decrease, and 1% showed a significant increase. Overall, the data indicated a clear trend of expanding heat risk zones, with the most significant changes concentrated around the city's central urban core.

#### 3.5.2. Space–Time Trend Pattern Division of Heat Exposure Risk at Night

According to Figure 10b, the proportion of areas with no significant change in nighttime population heat exposure risk in Xi'an has consistently remained high. This pattern shared certain similarities with the daytime distribution; however, the spatial continuity of the unchanged areas was more pronounced at night and was less affected by the expansion of the urban built-up area. As shown in Figure 10a, from 2003 to 2008, the areas with elevated risk levels at night were mainly concentrated within the central urban districts. Compared with the daytime distribution, the nighttime risk elevation zones during this period exhibited a higher degree of spatial clustering, without the fragmented and dispersed patterns observed in some daytime regions. From 2008 to 2013, the proportion of nighttime risk elevation areas decreased significantly. Unlike the daytime pattern, the spatial shift

in the risk center at night was less pronounced and did not exhibit an apparent outward expansion. Between 2013 and 2018, the center of increased nighttime population heat exposure risk shifted back to the central urban area, showing a tendency to expand toward the eastern, northern, and southern zones. From 2018 to 2023, zones with significantly elevated nighttime heat risk were mainly distributed in the core of the central urban area, with expansion trends toward the west, north, and south. Compared with the daytime distribution, the nighttime high-risk zones exhibited greater spatial compactness and clearer boundary contours.

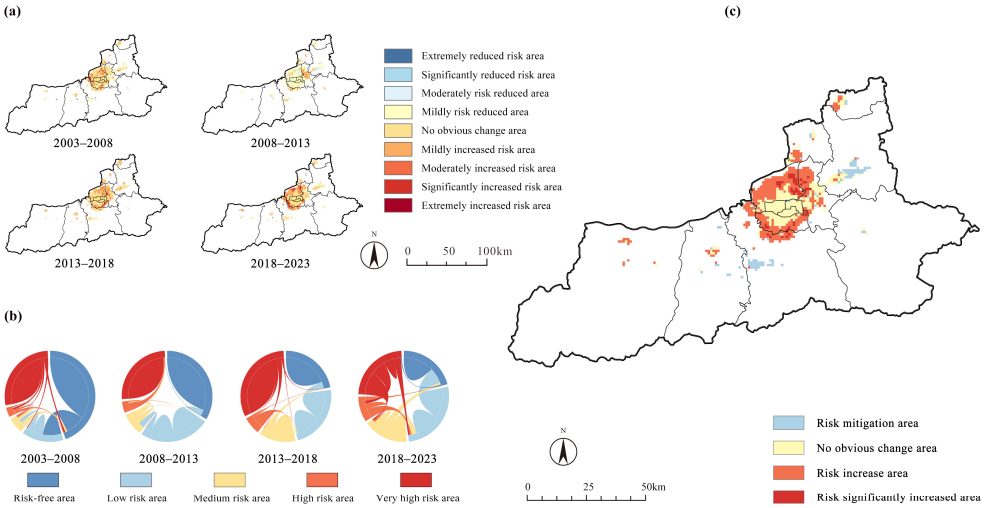


**Figure 10.** Spatial–temporal transfer and trend of heat exposure risk intensity of night population: (**a**) population heat exposure risk level changed at night in 5 years; (**b**) the mutual transformation between risk areas with low, medium, high, and very high risk levels and risk-free areas at night from 2003 to 2023; (**c**) the change in population heat exposure risk at night from 2003 to 2023.

As shown in Figure 10c, over the twenty years, the proportion of areas with no significant change in nighttime population heat exposure risk was 3.16%, while the risk mitigation zones accounted for 1.00%, risk increase zones for 4.37%, significant decrease zones for 0%, and significant increase zones for 0.49%. Overall, nighttime heat risk zones also showed an expanding trend; however, both the expansion rate and intensity were lower than during the day. Furthermore, the spatial center of expansion remained stably concentrated around the central urban core, without the leapfrog-type outward growth observed in some daytime periods.

## 4. Discussion

### *4.1. Potential Reasons for Changes in Urban Heat Island and Population Heat Exposure Distribution*

This study systematically analyzed the changes in the areal proportions of different levels of UHI zones and heat exposure risk areas in Xi'an during summer days and nights from 2003 to 2023. The results indicated that UHI intensity and heat exposure risk in Xi'an have generally increased over the 20 years. The proportions of non-UHI zones and no-risk areas have continually declined, whereas the proportions of strong UHI zones and high-risk areas (i.e., high and very high risk) expanded significantly. Spatially, strong UHI zones and high-risk areas were predominantly concentrated in the central urban districts and exhibited similar spatial distribution patterns.

Between 2013 and 2018, both daytime and nighttime UHI extents in Xi'an reached their maximum values within the 20 years, and the growth rate of UHI area proportions also peaked during this time. This trend was closely associated with the dramatic expansion of built-up areas during rapid urbanization and was consistent with the find-

ings of Liu, Han et al. [65,66]. The rapid expansion of urban built-up land into surrounding suburbs, combined with the concentrated growth of industrial production, traffic flow, and residential energy consumption, further intensifying anthropogenic heat emissions [67]. Consequently, carbon emissions in Xi'an increased from 45.11 million tons to 72.70 million tons between 2010 and 2021 [68]. In addition, the phased increase in average summer temperatures during this period [69] provided a climatic background that reinforced the heat island effect, leading to its peak under the synergistic influence of natural and anthropogenic factors. The growth rate of the nighttime heat island area peaked during 2008–2013, when the rapid expansion of built-up areas was primarily reflected in the concentrated construction of residential neighborhoods and commercial facilities. The widespread adoption of air conditioning, along with surges in nighttime cooling demand, lighting, and other domestic energy consumption, contributed to the peak rate of nighttime heat island expansion during this period [42]. The daytime and nighttime heat island ranges in Xi'an declined during 2018–2023. Similarly to the findings of Huo et al. [70], this decline was likely attributable to the implementation of urban thermal environment management policies and the promotion of ecological construction. A study by Song et al. [71] indicated that the core characteristic of Xi'an's spatial transformation from 2015 to 2020 was a structural shift from production and living spaces to ecological spaces; meanwhile, a study by Liu et al. [72] also confirmed that compared with 2015, Xi'an's Urban Ecological Quality (UEQ) showed a significant improvement trend in 2019. These studies collectively demonstrate that in recent years, Xi'an has gradually transitioned from a development model centered on economic benefits to a sustainable development model pursuing the coordination of ecological and financial benefits. This adjustment in development strategy directly promoted the continuous optimization of urban environmental quality after 2019, which was further reflected in the temporal and spatial evolution characteristics of UHI as a significant reduction in the spatial scope of diurnal and nocturnal UHI in Xi'an from 2018 to 2023. In addition, after the outbreak of the global COVID-19 pandemic in late 2019 and early 2020, Xi'an implemented human activity restriction measures, including the temporary shutdown of factories, to prevent and control the epidemic [73]. Existing studies [74,75] have confirmed that the reduction in anthropogenic heat emissions caused by such measures, although not the dominant factor in UHI mitigation, also contributed to a certain extent to the alleviation of the UHI effect in Xi'an in recent years.

The spatial and temporal evolution of the heat exposure risk of Xi'an was closely linked to the expansion of the urban heat island effect. The daytime heat risk zone share peaked in 2018, corresponding to the maximum extent of the heat island and the spatial distribution of population activities during that period. The nighttime thermal risk zone share peaked in 2023. This diurnal difference may be associated with human activity patterns: daytime anthropogenic heat sources, such as sub-urban industrial production and traffic emissions, promoted a more pronounced expansion of low- and medium-risk zones, whereas at night, the slow release of subsurface heat and weakened ventilation conditions sustained the growth of very high-risk zones. In 2008, the proportion of thermal risk zones during the daytime was lower than that in 2003. The main reason was the narrowing of the scope of low-risk zones, which was related to the decline in population density in the suburbs due to the urban siphoning effect of the central city in this period [6]. The coupling between population and thermal environment was reduced, resulting in the contraction of the scope of the low-risk zones. The overall proportion of thermal risk presented a phased and short-lived decline.

Compared with other Chinese urban heat island studies by Jia, Xu et al. [41,76], the increasing trend in heat exposure risk in Xi'an was consistent. However, the nighttime growth of its very high-risk zones was slightly lower than the daytime growth, which was

consistent with the Xi'an study by Yuan et al. [45] and reflected the distinctive differences between daytime and nighttime thermal environments in megacities. This study examined the dynamics of the heat island effect and population heat exposure risk in Xi'an using a 20-year time series of comparative diurnal and nocturnal analyses, thereby addressing the limitations of existing studies that focused solely on a single time period or the daytime thermal environment.

### *4.2. The Influence of Population Density and Heat Island Intensity on Population Heat Risk*

According to Figures 11a–c and 12a–c, the influence of UHI intensity and population density on population heat risk was identified as a complex interaction involving daytime and nighttime variations in Xi'an's heat island, population density, and heat risk between 2003 and 2023, with significant spatial and temporal differences observed. In terms of the overall effect, UHI intensity exerted a substantially greater impact on thermal risk than population density, because it directly determined the regional thermal environment. When the heat island effect intensified, the extent of the UHI area expanded accordingly. Even if population density remained stable, the number of people exposed to high temperatures increased due to the deteriorating thermal environment, thereby raising the overall heat exposure risk. The effect of population density was more evident in amplifying thermal risk, i.e., the denser the population in the same thermal environment, the larger the number of individuals exposed to high temperatures, and the greater the hazards posed by thermal risk.

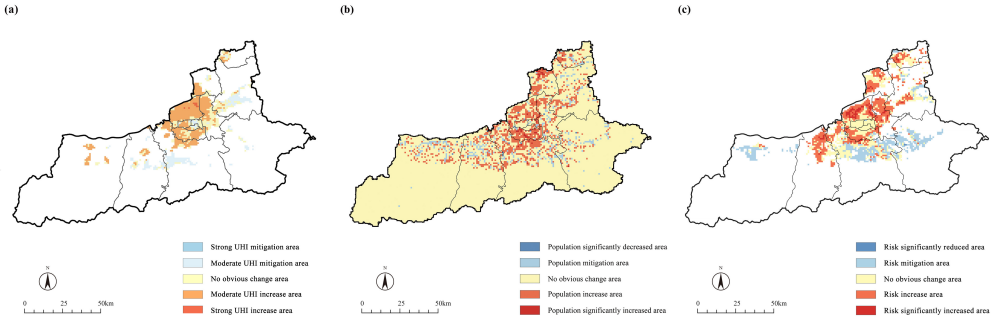


**Figure 11.** The effects of daytime population density and heat island intensity on population heat risk: (**a**) the change in UHI area during the daytime from 2003 to 2023; (**b**) the change in population density from 2003 to 2023; (**c**) the change in population heat exposure risk of daytime from 2003 to 2023.

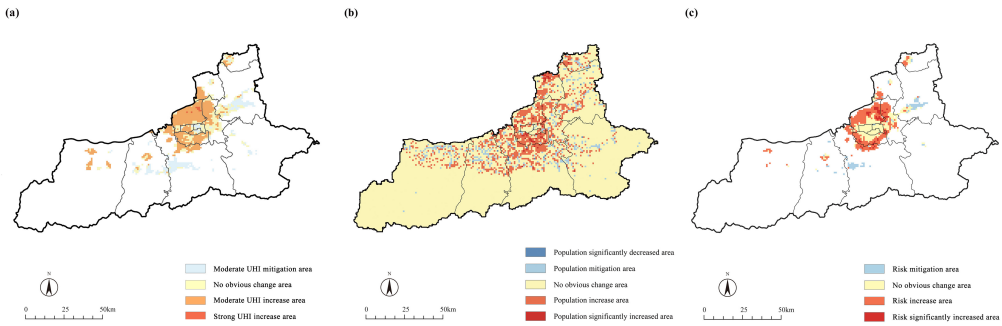


**Figure 12.** The impact of nighttime population density and heat island intensity on population thermal risk: (**a**) the change in UHI area at night from 2003 to 2023 (**b**) the change in population density from 2003 to 2023; (**c**) the change in population heat exposure risk at night from 2003 to 2023.

The spatial differences were even more pronounced. In the central city, heat risk was primarily dominated by UHI intensity due to long-term high population concentrations,

where even small increases in intensity were amplified into high risk by dense populations, making intensity the dominant factor. In contrast, risk changes in the peripheral southeastern part of the city were more dependent on population density, and instances often occurred where UHI intensity increased while population density remained relatively unchanged. This pattern occurred because the city's periphery mainly was in a transitional stage of urbanization, where population density was much lower than in the central city and stable population agglomerations had not yet formed. Even if UHI intensity increased due to local construction (e.g., industrial zone expansion or road hardening), thermal risk levels declined when population density did not increase or even decreased, because the number of people actually exposed to high temperatures was limited. Changes in the thermal environment often preceded population accumulation, reflecting the lagged nature of the shifts in population heat exposure risk.

Overall, the spatial and temporal coupling of heat island intensity and population density was an important influential factor driving the increase in population heat exposure risk. High-risk areas were primarily concentrated in zones where high population density overlapped with strong heat island intensity. Anthropogenic heat emissions resulting from population concentration further intensified the heat island effect. Simultaneously, the sustained high-temperature environment created by strong heat island intensity exposed dense populations to prolonged heat, ultimately generating a positive feedback loop of population concentration, heat island intensification, and escalating heat risk. The expansion of low- and medium-risk areas reflected the combined effects of the heat island spreading from the central city to the suburbs and the suburbanization of the population. The expansion of the heat island range gradually incorporated the suburbs into the high-temperature impact zone, while continuous population inflows accumulated heat exposure risk in these areas, ultimately forming a transition zone of escalating heat risk.

### *4.3. Research Deficiencies and Policy Recommendations*

Several limitations remain in this study, which require further improvement in subsequent research.

Regarding the application of population data, a single set of population data was used for the day–night comparison of population heat exposure risk in this study, with a data resolution of 1 km. While this setting limits the in-depth analysis of the diurnal variation in population heat exposure risk caused by commuting behavior, it also fails to capture the spatiotemporal trajectories of urban heat islands and population heat exposure risk at the neighborhood scale in Xi'an. However, it should be noted that the LandScan population data used in this study is currently the highest-precision public dataset available within the study area. The impact of the limitations above on the core conclusions, such as the intensification of population heat exposure risk in Xi'an and the expansion characteristics of diurnal and nocturnal UHI areas, is negligible. In the future, when population datasets with higher resolutions and including sociological attributes (e.g., age) are made publicly available, they can be deeply integrated with thermal environment monitoring data to further enhance the refinement level of heat exposure risk assessment.

This study only incorporated air temperature into the analysis of UHIs and heat exposure, without considering humidity as a key influencing factor. As a core variable regulating thermal comfort, the absence of humidity may result in an incomplete assessment of the actual thermal environment; nevertheless, this limitation does not alter the core judgment of this study regarding the spatiotemporal evolution trends of UHIs and population heat exposure risk in Xi'an. Future research can focus on exploring the coupling relationship between temperature and humidity, integrating humidity indicators into the calculation of

thermal comfort indices, and refining the heat exposure risk assessment model to better align with actual human perceptions.

Additionally, this study has not yet conducted an in-depth analysis of the quantitative relationship between land use types and thermal risk, which, to a certain extent, limits the depth of the study on the formation mechanism of UHIs. In the future, multiple regression models can be constructed to quantify the contributions of different land use types (e.g., green spaces, construction land, and water bodies) to the regional thermal environment, thereby providing more targeted spatial planning references for optimizing urban thermal environments.

Based on the conclusions of this study, the following policy recommendations were proposed to guide improvements in Xi'an's urban thermal environment and to support the prevention and control of population heat exposure risk. Differentiated thermal risk management should be implemented, with targeted measures tailored to the characteristics of specific areas. For core urban areas, such as the central city, reducing heat island intensity should be a top priority. For example, the layout of urban ventilation corridors should be optimized, so that air can circulate more smoothly to carry away heat [77,78]. Additionally, building reflectivity should be enhanced to reduce heat absorption [79]. In peripheral urban areas, the focus should be on controlling population concentration to avoid thermal stress from overcrowding, while simultaneously developing a comprehensive green space system to buffer heat exposure risk through the ecological functions of vegetation [80–82]. Differences between daytime and nighttime thermal environments should be considered, and distinct planning strategies should be developed. At night, because heat is not easily dispersed from the city center, heat dissipation should be enhanced by integrating urban trees into planning and design [83]. During the daytime, frequent population movements such as cross-district commuting increase the risk of heat exposure [84]. Therefore, the layout of public service facilities should be optimized to provide residents with easier access, thereby reducing unnecessary cross-district mobility and lowering commuting-related heat exposure. In addition, satellite remote sensing technology and ground-based observation networks can be integrated to develop a real-time thermal risk early warning platform based on a 1 km $\times$ 1 km grid. This system would enable real-time monitoring of regional thermal risk, with particular focus on areas where population and heat island intensity overlap strongly, thereby allowing timely preventive and control measures by relevant authorities [85].

## 5. Conclusions

Based on population density distribution data and diurnal surface temperature records for Xi'an from 2003 to 2023, this study systematically analyzed the spatiotemporal evolution of the summer heat island and population heat exposure risk. It examined the impacts of population growth and enhanced heat island intensity on the dynamics of thermal risk.

The results indicated the following: (1) The summer heat island effect and population heat exposure risk in Xi'an exhibited a general trend of intensification over the 20-year period. The proportions of non-heat island and no-risk areas continually decreased. In contrast, medium-intensity heat island zones (moderate and strong heat islands) and high-risk areas (high and very high risk) expanded significantly. The most pronounced increase occurred in the very high-risk areas, which entered an accelerated growth phase between 2018 and 2023. (2) Both population growth and increasing heat risk characterized the transformation of heat island and heat risk areas. These transformations showed an upgrading trend from lower to higher grades, while spatial expansion exhibited a radiation-like spread from high- to low-risk zones, with the central city as the core. (3) The trends in heat island and population heat exposure risk changes were generally consistent between

day and night, although the expansion of each grade of heat island and risk area at night was slightly lower than during the day. (4) Changes in the thermal environment often preceded population aggregation, indicating a lag effect in the evolution of heat exposure risks. (5) The coupling of population growth and heat island intensity was identified as the important influential factor driving the increase in population heat exposure risk. Continuous population growth in Xi'an led to increased anthropogenic heat emissions and hard surface expansion, which directly exacerbated the heat island effect. The intensification of the heat island further expanded both the scope and magnitude of population heat exposure, generating a positive feedback loop of population concentration, heat island intensification, and escalating heat risk.

This study revealed the influence of population and heat island factors on thermal risk, thereby providing a key scientific basis for urban thermal environment management in Xi'an. By clarifying the spatial coupling between population concentration and areas with strong heat island, corresponding prevention and control strategies can be developed. For example, the layout of green spaces and ventilation corridors in densely populated central districts should be optimized to mitigate heat island intensity, while ecological buffer zones should be planned to curb the expansion of heat risk zones in peri-urban areas where human activities are concentrated.

In addition, several limitations remain. This study employs the LandScan dataset, which has a 1 km spatial resolution for population data, making it challenging to conduct in-depth analysis of diurnal variations in heat exposure risk caused by commuting and other human activities, as well as the spatiotemporal evolution of urban heat islands (UHIs) and heat risk at the neighborhood scale. Additionally, it does not incorporate humidity into thermal environment analysis, nor does it consider the quantitative relationship between land use types and heat risk. However, the limitations above have a negligible impact on the core conclusions of this study.

Future research can integrate higher-resolution dynamic population data with thermal environment monitoring data, develop multivariate models to quantify the contribution of land use to the thermal environment, and establish a coupled risk assessment model that considers both population and UHIs. These efforts will provide more in-depth theoretical support for the precision regulation of population heat exposure risk in megacities.

**Supplementary Materials:** The following supporting information can be downloaded at: https://www.mdpi.com/article/10.3390/land14102021/s1, Table S1: Total population from census and LandScan data and the revised factors [55].

**Author Contributions:** Conceptualization, H.Z. and X.X.; methodology, H.Z., Z.L. and X.W.; software, H.Z., Z.L. and X.W.; validation, Z.L. and X.W.; formal analysis, Z.L. and X.W.; investigation, Z.L. and X.W.; resources, H.Z., Z.L. and X.W.; data curation, Z.L. and X.W.; writing—original draft preparation, Z.L. and X.W.; writing—review and editing, H.Z. and X.X.; visualization, Z.L. and X.W.; supervision, H.Z. and X.X.; project administration, H.Z. and X.X.; funding acquisition, X.X., Z.L. and X.W. contributed equally to this paper. All authors have read and agreed to the published version of the manuscript.

**Funding:** This research was funded by the Innovation and Entrepreneurship Training Program for College Students of Beijing Forestry University (Grant No. X202310022138) and the China Scholarship Council (Grant No. 202406510022).

**Data Availability Statement:** The main data used in this study include LST and population data. In this study, we obtained daytime and nighttime LST data for summer (June–August) for five time periods (2003, 2008, 2013, 2018, and 2023) from the MOD11A2 product released by MODIS (available on the GoogleEarthEngine cloud platform at https://code.earthengine.google.com/); the data were acquired through a dataset-specific API interface and were accessed on 2 July 2025. Population data for

the five time periods (2003, 2008, 2013, 2018, and 2023) used in this study were derived primarily from LandScan Global population distribution data (https://landscan.ornl.gov/, accessed on 28 June 2025) and Xi'an Statistical Yearbook population data (https://tjj.xa.gov.cn/tjnj/2024/zk/indexch.htm, accessed on 2 July 2025) [55].

**Acknowledgments:** In preparing this manuscript, the authors used Grammarly (Premium) and ChatGPT-5 to correct and polish the grammar used in translating Chinese manuscripts into English. The authors have reviewed and edited the output and take full responsibility for the content of this publication.

**Conflicts of Interest:** The authors declare no conflicts of interest.

## Abbreviations

The following abbreviations are used in this manuscript:

| | |
|---|---|
| LST | Land Surface Temperature |
| UHI | Urban Heat Island |
| LCZ | Local Climate Zones |
| SUHI | Surface Urban Heat Island |
| std | standard deviation |
| DI | Discomfort Index |
| UDI | UHI discomfort index |
| $EUHI_{raster}$ | UHI exposure index at the raster scale |

## References

1. Wu, Y.-C.; Lu, C.-L.; Lin, T.-P. Evaluating the effectiveness of tree canopy and building shade in urban heat mitigation using solar radiation transmittance. *Urban Clim.* **2025**, *62*, 102522. [CrossRef]
2. Liu, L.; Xia, B.; Zhang, L. Outdoor thermal comfort of urban river landscape belt in China's cold region: A case study of Xi'an. *Urban Clim.* **2023**, *48*, 101406. [CrossRef]
3. Yao, R.; Huang, X.; Zhang, Y.; Wang, L.; Li, J.; Yang, Q. Estimation of the surface urban heat island intensity across 1031 global cities using the regression-modification-estimation (RME) method. *J. Clean. Prod.* **2024**, *434*, 140231. [CrossRef]
4. Pérez, I.A.; García, M.Á.; Rasekhi, S.; Pazoki, F.; Fernández-Duque, B. Extension and trend of the London urban heat island under Lamb weather types. *Sustain. Cities Soc.* **2024**, *114*, 105743. [CrossRef]
5. Ming, Y.; Liu, Y.; Liu, X.; Tian, Z. Demographic disparity in diurnal surface urban Heat Island exposure across local climate zones: A case study of Chongqing, China. *Sci. Total Environ.* **2024**, *923*, 171203. [CrossRef]
6. Liu, D.; Zhou, R.; Ma, Q.; He, T.; Fang, X.; Xiao, L.; Hu, Y.; Li, J.; Shao, L.; Gao, J. Spatio-temporal patterns and population exposure risks of urban heat island in megacity Shanghai, China. *Sustain. Cities Soc.* **2024**, *108*, 105500. [CrossRef]
7. Masson, V.; Lemonsu, A.; Hidalgo, J.; Voogt, J. Urban Climates and Climate Change. *Annu. Rev. Environ. Resour.* **2020**, *45*, 411–444. [CrossRef]
8. Wang, B.; Gao, M.; Li, Y.; Li, Z.; Liu, Z.; Zhang, X.; Wen, Y. Unraveling the effects of extreme heat conditions on urban heat environment: Insights from local climate zones and integrated temperature data. *Sustain. Cities Soc.* **2025**, *122*, 106254. [CrossRef]
9. Galdies, C.; Lau, H.S. Urban Heat Island Effect, Extreme Temperatures and Climate Change: A Case Study of Hong Kong SAR. In *Climate Change,* Hazards and Adaptation Options: Handling the Impacts of a Changing Climate; Leal Filho, W., Nagy, G.J., Borga, M., Chávez Muñoz, P.D., Magnuszewski, A., Eds.; Springer: Berlin/Heidelberg, Germany, 2020; pp. 369–388. [CrossRef]
10. He, Y.; Wang, Z.; Wong, H.M.; Chen, G.; Ren, C.; Luo, M.; Li, Y.; Lee, T.-C.; Chan, P.W.; Ho, J.Y.-E.; et al. Spatial-temporal changes of compound temperature-humidity extremes in humid subtropical high-density cities: An observational study in Hong Kong from 1961 to 2020. *Urban Clim.* **2023**, *51*, 101669. [CrossRef]
11. Songsom, V.; Jaruk, P.; Suteerasak, T. Examining the spatiotemporal dynamics of urban heat island and its impact on air pollution in Thailand. *Environ. Chall.* **2025**, *19*, 101120. [CrossRef]
12. Ding, Y.; Feng, H.; Zou, B.; Nie, Y. Heterogeneous air pollution controls its correlation to urban heat island: A satellite perspective. *Adv. Space Res.* **2022**, *69*, 4252–4262. [CrossRef]
13. Chang, Y.; Guo, X. Disparities in the impact of urban heat island effect on particulate pollutants at different pollution stages—A case study of the "2 + 36" cities. *Urban Clim.* **2025**, *59*, 102273. [CrossRef]

14. Ebi, K.L.; Capon, A.; Berry, P.; Broderick, C.; de Dear, R.; Havenith, G.; Honda, Y.; Kovats, R.S.; Ma, W.; Malik, A.; et al. Hot weather and heat extremes: Health risks. *Lancet* **2021**, *398*, 698–708. [CrossRef]
15. Cleland, S.E.; Steinhardt, W.; Neas, L.M.; West, J.J.; Rappold, A.G. Corrigendum to "Urban heat island impacts on heat-related cardiovascular morbidity: A time series analysis of older adults in US metropolitan areas" [Environ. Int. 178 (2023) 108005]. *Environ. Int.* **2025**, *202*, 109613. [CrossRef]
16. Huang, H.; Deng, X.; Yang, H.; Zhou, X.; Jia, Q. Spatio-Temporal Mechanism Underlying the Effect of Urban Heat Island on Cardiovascular Diseases. *Iran. J. Public Health* **2020**, *49*, 1455–1466. [CrossRef]
17. Bi, X.; Wu, C.; Wang, Y.; Li, J.; Wang, C.; Hahs, A.; Mavoa, S.; Song, C.; Konrad, C.; Emch, M. Changes in the associations between heatwaves and human mortality during two extreme hot summers in Shanghai, China. *Sustain. Cities Soc.* **2023**, *95*, 104581. [CrossRef]
18. Yadav, N.; Rajendra, K.; Awasthi, A.; Singh, C.; Bhushan, B. Systematic exploration of heat wave impact on mortality and urban heat island: A review from 2000 to 2022. *Urban Clim.* **2023**, *51*, 101622. [CrossRef]
19. Yuan, Y.; Li, X.; Wang, H.; Geng, X.; Gu, J.; Fan, Z.; Wang, X.; Liao, C. Unraveling the global economic and mortality effects of rising urban heat island intensity. *Sustain. Cities Soc.* **2024**, *116*, 105902. [CrossRef]
20. Jia, W.; Ren, G.; Jin, F.; He, J.; Zhang, P. Spatial-temporal characteristics of the urban heat island effect in Xiamen, China. *Urban Clim.* **2023**, *52*, 101725. [CrossRef]
21. Qiao, X.; Liu, L.; Li, Y.; Yang, Y.; Dai, Y.; Zhang, J.; Zhang, J.; Zheng, J.; Zhao, S. Spatio-temporal evolution and simulation prediction of heat island effect in shrinking cities in China based on improved CA-Markov modeling. *Sustain. Cities Soc.* **2025**, *130*, 106583. [CrossRef]
22. Yin, S.; Xiao, S.; Ding, X.; Fan, Y. Improvement of spatial-temporal urban heat island study based on local climate zone framework: A case study of Hangzhou, China. *Build. Environ.* **2024**, *248*, 111102. [CrossRef]
23. Peng, X.; Zhou, Y.; Fu, X.; Xu, J. Study on the spatial-temporal pattern and evolution of surface urban heat island in 180 shrinking cities in China. *Sustain. Cities Soc.* **2022**, *84*, 104018. [CrossRef]
24. Xu, H.; Li, C.; Hu, Y.; Kong, R.; Wang, Q.; Zhou, Y. Long-term temporal and spatial divergence patterns of urban heat risk in the Beijing–Tianjin–Hebei urban agglomeration. *Urban Clim.* **2024**, *56*, 102085. [CrossRef]
25. Badugu, A.; Arunab, K.; Mathew, A.; Sarwesh, P. Spatial and temporal analysis of urban heat island effect over Tiruchirappalli city using geospatial techniques. *Geod. Geodyn.* **2023**, *14*, 275–291. [CrossRef]
26. Amorim, M.C.d.C.T.; Dubreuil, V.; Teixeira, D.C.F.; Amorim, A.T.; Brabant, C. Exceptional heat island intensities also occur in medium-sized cities. *Urban Clim.* **2024**, *53*, 101821. [CrossRef]
27. Wang, C.; Chen, J.; Wang, Q.; Li, D.; Zhu, M.; Gan, Z.; Qin, M.; Zhang, Y. The polycentricity of urban population will lead to improvements in urban heat island effect: Evidence from the Yangtze river delta in China. *Sustain. Futures* **2025**, *9*, 100510. [CrossRef]
28. Zhang, H.; Wang, C.; Yang, H.; Ma, Z. How do morphology factors affect urban heat island intensity? an approach of local climate zones in a fast-growing small city, Yangling, China. *Ecol. Indic.* **2024**, *161*, 111972. [CrossRef]
29. Liu, W.; Zhao, H.; Sun, S.; Xu, X.; Huang, T.; Zhu, J. Green Space Cooling Effect and Contribution to Mitigate Heat Island Effect of Surrounding Communities in Beijing Metropolitan Area. *Front. Public Health* **2022**, *10*, 870403. [CrossRef]
30. Lai, J.; Zhan, W.; Voogt, J.; Quan, J.; Huang, F.; Zhou, J.; Bechtel, B.; Hu, L.; Wang, K.; Cao, C.; et al. Meteorological controls on daily variations of nighttime surface urban heat islands. *Remote Sens. Environ.* **2021**, *253*, 112198. [CrossRef]
31. Yang, H.; Wu, Z.; Qiu, S.; Wu, F.; Dawson, R.J.; Ford, A.; Barr, S. Surface urban heat island variations under the 3-decadal urban expansion in China: Patterns and driving factors. *Sustain. Cities Soc.* **2025**, *130*, 106640. [CrossRef]
32. Li, H.; Zhou, Y.; Jia, G.; Zhao, K.; Dong, J. Quantifying the response of surface urban heat island to urbanization using the annual temperature cycle model. *Geosci. Front.* **2022**, *13*, 101141. [CrossRef]
33. Macintyre, H.L.; Heaviside, C.; Cai, X.; Phalkey, R. The winter urban heat island: Impacts on cold-related mortality in a highly urbanized European region for present and future climate. *Environ. Int.* **2021**, *154*, 106530. [CrossRef] [PubMed]
34. Qian, J.; Zhang, L.; Schlink, U.; Hu, X.; Meng, Q.; Gao, J. Impact of urban land use and anthropogenic heat on winter and summer outdoor thermal comfort in Beijing. *Urban Clim.* **2025**, *59*, 102306. [CrossRef]
35. Liang, T.; He, J.; Chen, L.; Yao, Z.; Zhang, L.; Che, H.; Gong, S. Simulation of the influence of a fine-scale urban underlying surface on the urban heat island effect in Beijing. *Atmos. Res.* **2021**, *262*, 105786. [CrossRef]
36. Jandaghian, Z.; Arasteh, H.; Heidari, D.; Ghobadi, M.; Lacasse, M.; Gover, B. Cool wall claddings for a sustainable future: A comprehensive review on mitigating urban heat island effects and reducing carbon emissions in the built environment. *Energy Build.* **2025**, *336*, 115600. [CrossRef]
37. Sheng, T.; Zhang, Z.; Qian, Z.; Ma, P.; Xie, W.; Zeng, Y.; Zhang, K.; Sun, Z.; Yu, J.; Chen, M. Examining urban agglomeration heat island with explainable AI: An enhanced consideration of anthropogenic heat emissions. *Urban Clim.* **2025**, *59*, 102251. [CrossRef]

38. Zhang, S.; Breitner, S.; Stafoggia, M.; de'Donato, F.; Samoli, E.; Zafeiratou, S.; Katsouyanni, K.; Rao, S.; Diz-Lois Palomares, A.; Gasparrini, A.; et al. Effect modification of air pollution on the association between heat and mortality in five European countries. *Environ. Res.* **2024**, *263*, 120023. [CrossRef] [PubMed]
39. Zhang, Q.; Jia, B.; Li, T.; Yang, Y.; Fang, Y. Dynamic changes and drives of surface urban heat islands in China. *City Environ. Interact.* **2025**, *27*, 100203. [CrossRef]
40. Zhang, Q.; Gu, L.; Jia, B.; Fang, Y. Summertime compound heat extremes change and population heat exposure distribution in China. *J. Clean. Prod.* **2024**, *485*, 144381. [CrossRef]
41. Jia, R.; Liu, J.; He, T.; Han, D.; Xu, X.; Liu, L.; Sun, Z.; Qiao, Z. Population heat exposure risk from the perspective of urban heat island spatial expansion in China during 2005–2020. *Urban Clim.* **2024**, *56*, 101987. [CrossRef]
42. Huang, X.; Li, L.; Yan, X.; Ji, W.; Zhao, K.; Zhao, X. Assessment of heat exposure risk for urban populations and spatio-temporal patterns: A perspective of urban functional zones in Xi'an, China. *Urban Clim.* **2024**, *55*, 101992. [CrossRef]
43. Zhao, K.; Ning, Z.; Xu, C.; Zhao, X.; Huang, X. How do driving factors affect the diurnal variation of land surface temperature across different urban functional blocks? A case study of Xi'an, China. *Sustain. Cities Soc.* **2024**, *114*, 105738. [CrossRef]
44. Zhao, S.; Dong, J.; Guo, F.; Zhang, H.; Zhu, P. Optimization of green space in high-density built-up areas based on cooling simulations: A case study in Xi'an, China. *Urban Clim.* **2024**, *58*, 102225. [CrossRef]
45. Yuan, B.; Zhou, L.; Hu, F.; Zhang, Q. Diurnal dynamics of heat exposure in Xi'an: A perspective from local climate zone. *Build. Environ.* **2022**, *222*, 109400. [CrossRef]
46. Yan, X.; Liu, J.; Zhang, W.; Wang, Z.; Jia, R.; Wang, L.; Liu, N.; Zhu, Y. Examination of green roofs' cooling effects in a big city based on multi-source remote sensing data: An example from central Xi'an, China. *Sustain. Cities Soc.* **2025**, *130*, 106545. [CrossRef]
47. Samra, R.M.A. Investigating and mapping day-night urban heat island and its driving factors using Sentinel/MODIS data and Google Earth Engine. Case study: Greater Cairo, Egypt. *Urban Clim.* **2023**, *52*, 101729. [CrossRef]
48. Si, M.; Li, Z.-L.; Nerry, F.; Tang, B.-H.; Leng, P.; Wu, H.; Zhang, X.; Shang, G. Spatiotemporal pattern and long-term trend of global surface urban heat islands characterized by dynamic urban-extent method and MODIS data. *ISPRS J. Photogramm. Remote Sens.* **2022**, *183*, 321–335. [CrossRef]
49. Mandal, J.; Patel, P.P.; Samanta, S. Examining the expansion of Urban Heat Island effect in the Kolkata Metropolitan Area and its vicinity using multi-temporal MODIS satellite data. *Adv. Space Res.* **2022**, *69*, 1960–1977. [CrossRef]
50. Kyaw, A.K.; Hamed, M.M.; Kamruzzaman, M.; Shahid, S. Spatiotemporal changes in population exposure to heat stress in South Asia. *Sustain. Cities Soc.* **2023**, *93*, 104544. [CrossRef]
51. Zhang, X.; Chang, L.; Wang, M.; Stein, A. Measuring polycentric urban development with multi-temporal Sentinel-1 SAR imagery: A case study in Shanghai, China. *Int. J. Appl. Earth Obs. Geoinf.* **2023**, *121*, 103340. [CrossRef]
52. Jaber, S.M. Is there a relationship between human population distribution and land surface temperature? Global perspective in areas with different climatic classifications. *Remote Sens. Appl. Soc. Environ.* **2020**, *20*, 100435. [CrossRef]
53. Liu, L.; Cao, X.; Li, S.; Jie, N. A 31-year (1990–2020) global gridded population dataset generated by cluster analysis and statistical learning. *Sci. Data* **2024**, *11*, 124. [CrossRef]
54. Zhao, H.; Fang, Y.; Xu, X. Quantifying morphology evolutions of urban heat islands and assessing their heat exposure in a metropolis. *Sustain. Cities Soc.* **2024**, *102*, 105244. [CrossRef]
55. Xi'an Statistical Yearbook 2024. Available online: https://tjj.xa.gov.cn/tjnj/2024/zk/indexch.htm (accessed on 25 August 2025).
56. Fernandes, R.; Nascimento, V.; Freitas, M.; Ometto, J. Local Climate Zones to Identify Surface Urban Heat Islands: A Systematic Review. *Remote Sens.* **2023**, *15*, 884. [CrossRef]
57. Dutta, K.; Basu, D.; Agrawal, S. Evaluation of seasonal variability in magnitude of urban heat islands using local climate zone classification and surface albedo. *Int. J. Environ. Sci. Technol.* **2021**, *19*, 8677–8698. [CrossRef]
58. Yuan, S.; Ren, Z.; Shan, X.; Deng, Q.; Zhou, Z. Seasonal different effects of land cover on urban heat island in Wuhan's metropolitan area. *Urban Clim.* **2023**, *49*, 101547. [CrossRef]
59. Kachar, H.; Vafsian, A.R.; Modiri, M.; Enayati, H.; Safdari Nezhad, A.R. Evaluation of Spatial and Temporal Distribution Changes of Lst Using Landsat Images (Case Study: Tehran). *Int. Arch. Photogramm. Remote Sens. Spat. Inf. Sci.* **2015**, *XL-1/W5*, 351–356. [CrossRef]
60. Polydoros, A.; Cartalis, C. Use of Earth Observation based indices for the monitoring of built-up area features and dynamics in support of urban energy studies. *Energy Build.* **2015**, *98*, 92–99. [CrossRef]
61. Wu, S.; Yu, W.; Chen, B. Observed inequality in thermal comfort exposure and its multifaceted associations with greenspace in United States cities. *Landsc. Urban Plan.* **2023**, *233*, 104701. [CrossRef]
62. Aram, F.; Solgi, E.; Garcia, E.H.; Mosavi, A. Urban heat resilience at the time of global warming: Evaluating the impact of the urban parks on outdoor thermal comfort. *Environ. Sci. Eur.* **2020**, *32*, 117. [CrossRef]
63. Bin, Z.O.U.; Fen, P.; Limin, J.; Min, W. GIS Aided Spatial Zoning of High\|Resolution Population Exposure to Air Pollution. *Geomat. Inf. Sci. Wuhan Univ.* **2013**, *38*, 334–338.

64. Zhao, X.; Zhao, K.; Huang, X. Population exposure risk to urban extreme heat environment based on ECOSTRESS land surface temperature and mobile phone signaling data: A case study of Xi'an City. *Prog. Geogr.* **2022**, *41*, 2061–2072. [CrossRef]
65. Liu, S.; Zang, Z.; Wang, W.; Wu, Y. Spatial-temporal evolution of urban heat Island in Xi'an from 2006 to 2016. *Phys. Chem. Earth Parts A/B/C* **2019**, *110*, 185–194. [CrossRef]
66. Han, B.; Luo, Z.; Liu, Y.; Zhang, T.; Yang, L. Using Local Climate Zones to investigate Spatio-temporal evolution of thermal environment at the urban regional level: A case study in Xi'an, China. *Sustain. Cities Soc.* **2022**, *76*, 103495. [CrossRef]
67. Luo, H.; Gao, X.; Liu, Z.; Liu, W.; Li, Y.; Meng, X.; Yang, X.; Yan, J.; Sun, L. Real-time Characterization Model of Carbon Emissions Based on Land-use Status: A Case Study of Xi'an City, China. *J. Clean. Prod.* **2023**, *434*, 140069. [CrossRef]
68. Liu, Z.; Han, L.; Liu, M. High-resolution carbon emission mapping and spatial-temporal analysis based on multi-source geographic data: A case study in Xi'an City, China. *Environ. Pollut.* **2024**, *361*, 124879. [CrossRef]
69. Xu, D.; Zhou, D.; Wang, Y.; Meng, X.; Chen, W.; Yang, Y. Temporal and spatial variations of urban climate and derivation of an urban climate map for Xi'an, China. *Sustain. Cities Soc.* **2020**, *52*, 101850. [CrossRef]
70. Huo, K.; Qin, R.; Zhao, J.; Ma, X. Long-term tracking of urban structure and analysis of its impact on urban heat stress: A case study of Xi'an, China. *Ecol. Indic.* **2025**, *174*, 113418. [CrossRef]
71. Song, J.; Lei, J.; Wang, P. Evolution of the "Production-Living-Ecological" space of urban trituration and its prediction of carbon mitigation potential–The case of Xi'an. *Ecol. Indic.* **2025**, *171*, 113137. [CrossRef]
72. Liu, M.; Ma, M.; Liu, J.; Lu, X.; Dong, Z.; Li, J. Quantifying impacts of natural and anthropogenic factors on urban ecological quality changes: A multiscale survey in Xi'an, China. *Ecol. Indic.* **2023**, *153*, 110463. [CrossRef]
73. Ali, G.; Abbas, S.; Qamer, F.M.; Wong, M.S.; Rasul, G.; Irteza, S.M.; Shahzad, N. Environmental impacts of shifts in energy, emissions, and urban heat island during the COVID-19 lockdown across Pakistan. *J. Clean. Prod.* **2021**, *291*, 125806. [CrossRef] [PubMed]
74. Meng, Q.; Qian, J.; Schlink, U.; Zhang, L.; Hu, X.; Gao, J.; Wang, Q. Anthropogenic heat variation during the COVID-19 pandemic control measures in four Chinese megacities. *Remote Sens. Environ.* **2023**, *293*, 113602. [CrossRef]
75. Gao, J.; Meng, Q.; Zhang, L.; Hu, X.; Hu, D.; Qian, J. Modeling the impact of pandemic on the urban thermal environment over megacities in China: Spatiotemporal analysis from the perspective of heat anomaly variations. *Int. J. Appl. Earth Obs. Geoinf.* **2025**, *136*, 104396. [CrossRef]
76. Xu, Y.; Jia, R.; Liu, J.; Han, D.; He, T.; Xu, X.; Liu, L.; Sun, Z.; Qiao, Z. The population exposure risk of urban heat island effect: From the perspective of urban spatial expansion in China. *Build. Environ.* **2024**, *258*, 111565. [CrossRef]
77. Fang, Y.; Zhao, L.; Dou, B.; Li, Y.; Wang, S. Circuit VRC: A circuit theory-based ventilation corridor model for mitigating the urban heat islands. *Build. Environ.* **2023**, *244*, 110786. [CrossRef]
78. Guan, S.; Zhang, X.; Zhang, T.; Hu, H. Considering the supply and demand of urban heat island mitigation: A study on the construction of "Source-flow-sink" cooling corridor network of blue and green landscape. *Ecol. Indic.* **2025**, *174*, 113448. [CrossRef]
79. Yuan, J.; Yan, D.; Xiao, X.; Shimazaki, Y.; Wang, Y.; Jiao, Z.; Lin, Z.; Bizjak, M.; Farnham, C.; Emura, K. Mitigating urban heat islands: Enhancing outdoor comfort with retro-reflective building materials through computational-fluid-dynamics analysis. *Next Res.* **2025**, *2*, 100199. [CrossRef]
80. Fang, Z.; Zhang, F.; Guo, Z.; Zheng, Z.; Feng, X. Investigation into the outdoor thermal comfort on different urban underlying surfaces. *Urban Clim.* **2024**, *55*, 101911. [CrossRef]
81. Xu, J.; Jin, Y.; Ling, Y.; Sun, Y.; Wang, Y. Exploring the seasonal impacts of morphological spatial pattern of green spaces on the urban heat island. *Sustain. Cities Soc.* **2025**, *125*, 106352. [CrossRef]
82. Yang, C.; Qin, Y.; Wu, H.; Zhao, Y.; Che, S. Urban park green spaces and their potential in regulating urban heat Island (UHI) effects in urban-rural gradient in Shanghai, China. *Sustain. Cities Soc.* **2025**, *129*, 106467. [CrossRef]
83. Jato-Espino, D.; Lierow, S.; Rodríguez-Sánchez, M. Using classification algorithms to model nighttime Surface Urban Heat Island (SUHI), with an emphasis on the role of urban trees. *Build. Environ.* **2025**, *270*, 112572. [CrossRef]
84. Danes, V.R.; Pinontoan, O.R.; Porajow, Z.C.; Simanjuntak, C.K.; Pasassung, F.; Sunarno, F.A.; Lempas, R.P.; Sumakud, V.J.; Simangunsong, V.; Pangaribuan, M. Impact of particulate matter and heat stress on cardiovascular health during traffic exposure. *Atmos. Pollut. Res.* **2025**, *16*, 102410. [CrossRef]
85. Castro, J.R.R.; Delina, L.L. The social, technological, economic, and political roles of information and communication technologies in extreme heat adaptation in urban Southeast Asia. *Urban Clim.* **2025**, *62*, 102556. [CrossRef]


**Disclaimer/Publisher's Note:** The statements, opinions and data contained in all publications are solely those of the individual author(s) and contributor(s) and not of MDPI and/or the editor(s). MDPI and/or the editor(s) disclaim responsibility for any injury to people or property resulting from any ideas, methods, instructions or products referred to in the content.